Mechanics of Materials 164 (2022) 104098

Contents lists available at ScienceDirect

Mechanics of Materials

journal homepage: www.elsevier.com/locate/mecmat

Invited paper

Three-dimensional stress state during dynamic shear rupture propagation along frictional interfaces in elastic plates

R. Rezakhani [a,b], V. Rubino [c,*], J.F. Molinari [b], A. Rosakis [c]

[a] Department of Mechanical Engineering and Material Science, Duke University, Durham, NC, USA
[b] Civil Engineering Institute, Materials Science and Engineering Institute, Ecole Polytechnique Fédérale de Lausanne (EPFL), Lausanne, Switzerland
[c] Graduate Aerospace Laboratories, California Institute of Technology, Pasadena, CA, USA

ARTICLE INFO

Keywords:
Dynamic shear ruptures
Friction
Finite element method

ABSTRACT

The state of stress in plates, where one geometric dimensions is much smaller than the others, is often assumed to be of plane stress. This assumption is justified by the fact that the out-of-plane stress components are zero on the free-surfaces of a plate to satisfy the boundary conditions, and have little chance to develop in the bulk, due to the small thickness of the plate. At the same time, it is known that the static stress field associated with cracks approximates plane-strain conditions in the near-crack tip. However, it is not clear how the pre-existing plane-stress field of a plate is modified by a propagating dynamic shear rupture. Here we study the particle velocities and stress fields of dynamic shear ruptures in mode II propagating along the predefined frictional interface of two plates of an elastic material, loaded in compression and shear, using three-dimensional finite element modeling. The numerical simulations show the rapid development of out-of-plane stresses in the interior of the specimen, between the free surfaces. The out-of-plane normal stress is characterized by an anti-symmetric pattern with lobes of alternating polarity, in planes parallel to the free-surfaces. On the interface plane, the out-of-plane stress has a complex pattern exhibiting an initial sudden variation over the plane-stress conditions followed by crisscrossing features, behind the rupture tip. This study shows how plane-stress conditions, defining the state of stress before rupture arrival, are suddenly altered during dynamic rupture propagation. The out-of-plane stress rapidly deviates from the free-surface condition and a state of equivalent plane-strain in the stress-changes field is attained at the rupture tip, while behind the rupture tip a fully three-dimensional stress state is established. The three-dimensional finite element simulations presented here help interpret and explain previous experiments of dynamic shear ruptures by showing the complex particle velocity and stress fields in the interior of the specimen and along the interface plane, which are currently not accessible to full-field experimental measurements.

1. Introduction

Dynamic shear cracks are relevant to a wide range of fields spanning from engineering to geophysics (Freund, 1998; Scholz, 2019). Some applications include fiber pull-out in the failure of composite materials (Tsai et al., 2005), bimaterial structures (Rosakis et al., 1998), vehicle brake systems (Liu and Chen, 2016), and earthquakes (Rice, 1983; Kanamori and Brodsky, 2004). Dynamic shear cracks have been the object of several theoretical, numerical, and experimental studies (Freund, 1998; Needleman, 1999; Rosakis et al., 2007; Liu and Lapusta, 2008; Ben-David et al., 2010; Passelegue et al., 2013; Fineberg and Bouchbinder, 2015; Kammer et al., 2015; Bayart et al., 2016; Rubino et al., 2019, 2020; Barras et al., 2019, 2020; Brun et al., 2020; Fekak et al., 2020; Rezakhani et al., 2020; Rosakis et al., 2020; Svetlizky et al., 2020). In theoretical studies, the state of stress is often assumed to be two-dimensional, typically plane strain for analytical models and either plane strain or plane stress in numerical simulations, depending on the geometry (Needleman, 1999; Coker et al., 2005; Shi et al., 2008). In plates, the stress state is normally assumed to be plane stress, due to the fact that the out-of-plane stress components are zero on the free surfaces to satisfy the boundary conditions, and due to small thickness of the plate compared to the other dimensions. However, crack propagation perturbs this state of stress, also affecting the behavior of other field quantities. The degree of stress three-dimensionality of crack fields in plates has been object of previous investigations for mode I cracks, particularly with reference on the interpretation of experiments with the techniques of caustics and Coherent Gradient Sensing (CGS) (Rosakis and Ravi-Chandar, 1986; Rosakis et al., 1990;

* Corresponding author.
E-mail address: vito.rubino@caltech.edu (V. Rubino).

https://doi.org/10.1016/j.mechmat.2021.104098
Received 14 May 2021; Received in revised form 20 August 2021; Accepted 29 September 2021
Available online 9 October 2021

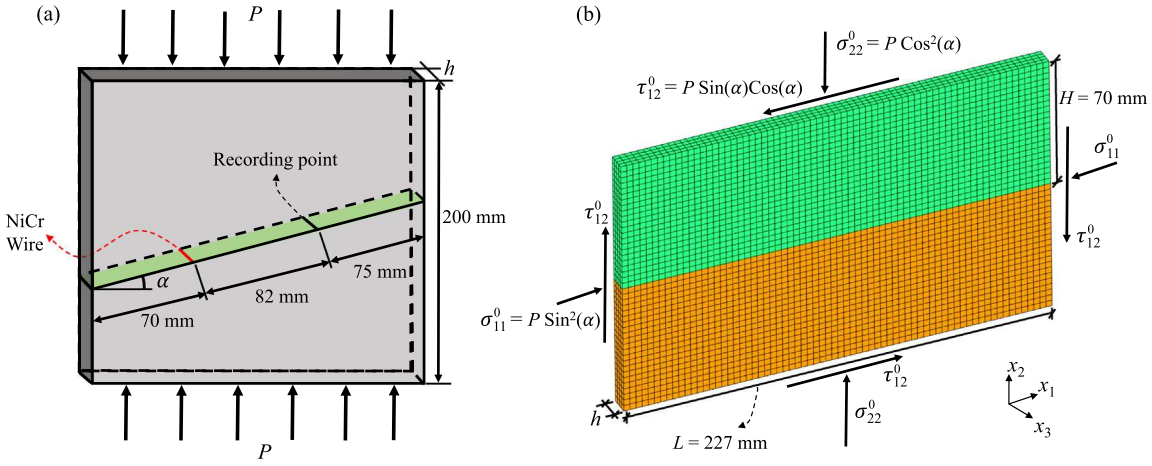

Fig. 1. (a) Schematic of the laboratory experimental setup, where dynamic ruptures propagate along the frictional interface of two plates of thickness h = 10 mm. The vertical loading produces interface-normal and shear pre-stresses on the interface inclined by an angle α. Ruptures are nucleated in the lab by the small burst of a NiCr wire placed across the interface. (b) A generic finite element mesh generated to illustrate the model. A coarse finite element discretization is used in the illustration for the sake of clarity. In the finite element simulation, linear hexahedral elements of 0.45 mm size are employed, discretizing the interface in x_1 direction with 500 elements. The simulations consider two different thicknesses h = 10 and 20 mm. The origin of the reference system is located at the intersection of the interface plane, and the two midplanes, such that the two larger free-surfaces are located at $x_3 = \pm h$.

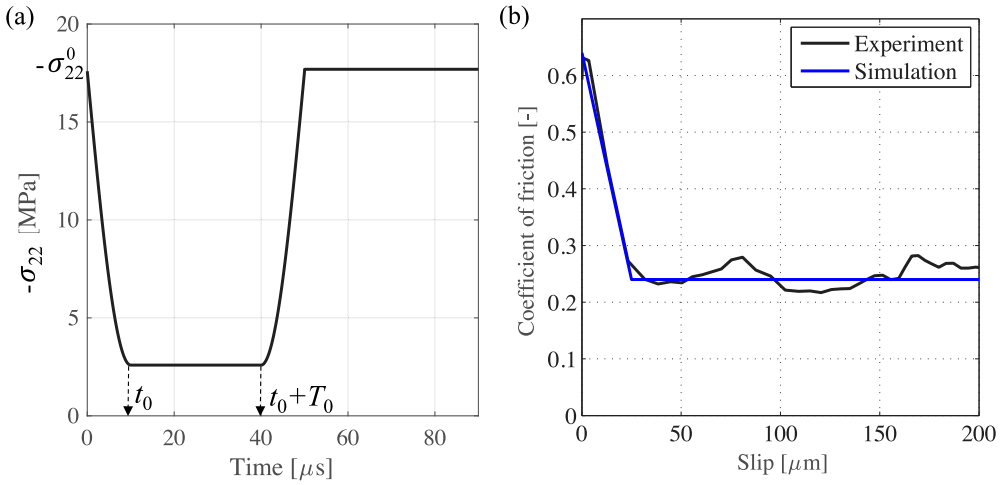

Fig. 2. (a) Evolution of the interface-normal stress as a result of the pressure transient on the nucleation zone to trigger rupture propagation. (b) Coefficient of friction measured in laboratory experiments (Rubino et al., 2017) and the idealized slip-weakening law implemented in the numerical simulations.

Zehnder and Rosakis, 1990; Lee and Rosakis, 1993). These studies revealed the prevalence of plane-stress state at distances larger than half thickness from the crack tip, and a three-dimensional stress state in the near-tip field, approaching plane strain at the crack tip. While three-dimensional simulations have studied the near-tip fields of shear cracks (Svetlizky et al., 2020), the stress state of dynamic cracks in mode II has not been thourougly investigated so far. In particular, it is not clear how the propagation of dynamic shear cracks results in the emergence of the out-of-plane stress component and how this affects the displacement and velocity fields. Shear cracks can propagate along coherent or incoherent interfaces. Coherent interfaces are characterized by finite strength and toughness and can resist opening and shear, while incoherent interfaces are governed by the frictional strength of the interface (Rosakis et al., 2007). In this paper, we study numerically the state of stress in the interior of a specimen with a plate configuration, during the propagation of dynamic frictional ruptures along a preexistent interface using finite element simulations. The finite element model replicates the key ingredients of dynamic ruptures propagating in the specimens used in the laboratory configurations of Rosakis and co-workers (Rosakis et al., 2007, 2020), and allows us to extend the parameter space over the experimental range, and to study the effect of thickness on the state of stress.

In the laboratory configuration studied, dynamic shear cracks are produced as frictional ruptures propagating along the interface made by two plates of a polymeric material (typically Homalite-100 or PMMA), inclined by an angle α (Fig. 1a) (Rubino et al., 2019; Rosakis et al., 2020). A compressive, vertical load P is applied on the specimen top and bottom faces and produces resolved normal and shear pre-stress components on the interface, given by $\sigma_n^0 = P\cos^2\alpha$ and $\tau^0 = P\cos\alpha\sin\alpha$, respectively. Dynamic ruptures are initiated by the sudden pressure release of a thin electric wire placed across the interface. This laboratory setup has been used to mimic earthquake ruptures propagating as shear cracks along pre-existing faults in the Earth's crust and it has been instrumental to study key earthquake physics issues, at first using diagnostics based on photoelasticity and laser velocimetry (Xia et al., 2004; Rosakis et al., 2007; Mello et al., 2010; Gabuchian et al., 2017), and recently using digital image correlation (Rubino et al., 2015, 2017; Gori et al., 2018; Rubino et al., 2019; Tal et al., 2019; Rosakis et al., 2020; Rubino et al., 2020; Tal et al., 2020). In particular, the present experimental configuration of the setup featuring ultrahigh-speed photography coupled with 2D digital image correlation (DIC)

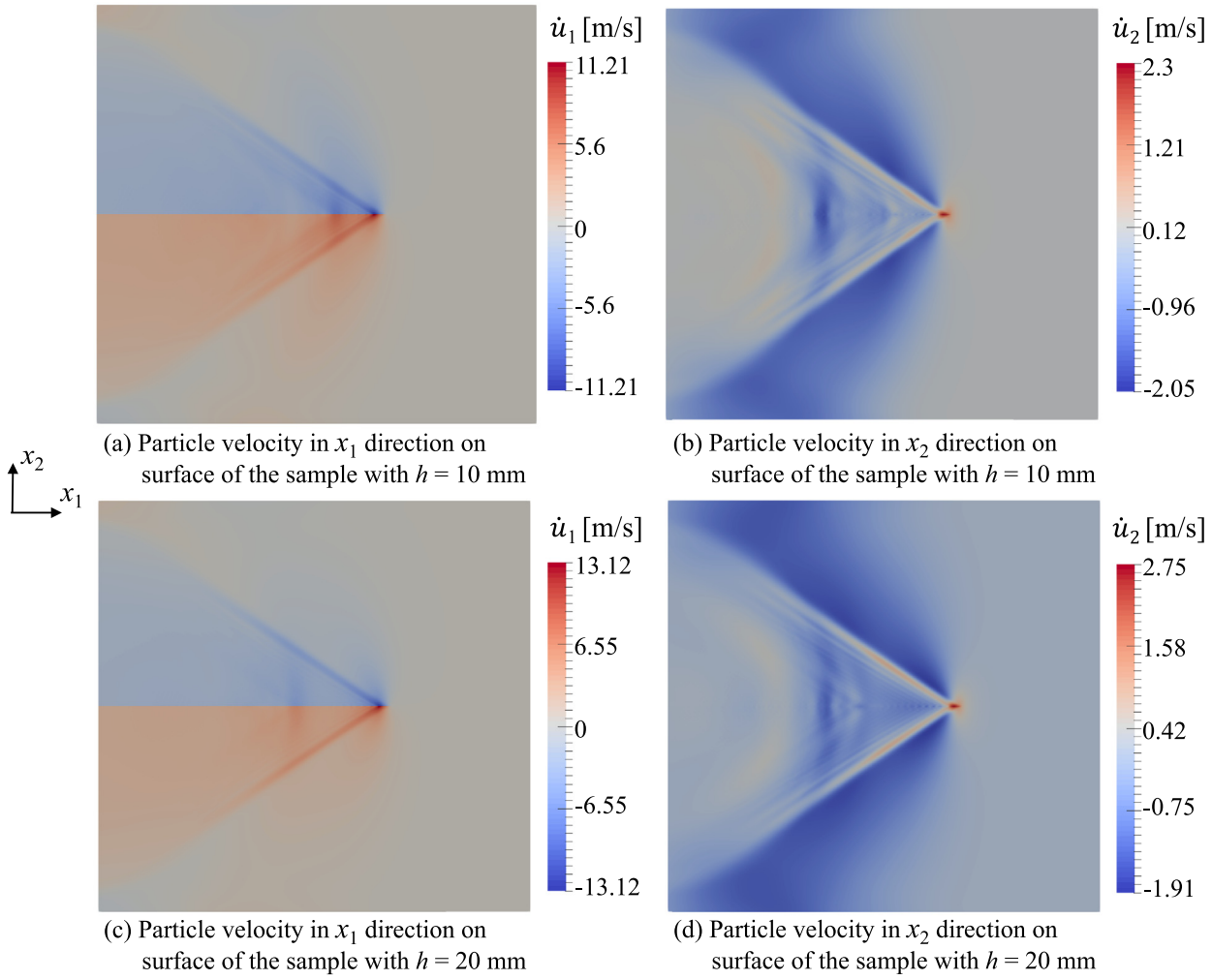

(a) Particle velocity in x_1 direction on surface of the sample with $h = 10$ mm

(b) Particle velocity in x_2 direction on surface of the sample with $h = 10$ mm

(c) Particle velocity in x_1 direction on surface of the sample with $h = 20$ mm

(d) Particle velocity in x_2 direction on surface of the sample with $h = 20$ mm

Fig. 3. Snapshots of the in-plane particle velocity fields $\dot{u}_1$ (left) and $\dot{u}_2$ (right) on the free-surface ($x_3 = h/2$) at $t = 54$ μs, for the case of $h = 10$ mm (a, b) and $h = 20$ mm (c, d). The ranges of in-plane axes in the maps are $80 < x_1 < 227$ mm and $-70 < x_2 < 70$ mm. Both velocity fields display sharp features associated with the formation of shear Mach fronts during supershear rupture propagation. A secondary peak in $\dot{u}_1$ appears along the interface behind the rupture tip and is linked to the propagation of the Mach features through the plate thickness, as explained in the text.

allows the measurement of the in-plane full-field displacements, particle velocities and strains, as well as stresses on the specimen's outer surface (Rubino et al., 2019; Rosakis et al., 2020). However, the current experimental configuration does not allow to measure field quantities in the interior of the specimen. Also, as these measurements are based on a 2D-DIC approach, they cannot capture the distribution of the out-of-plane components. Previous numerical simulations of this setup assumed a plane-stress state (Lu et al., 2009; Mello et al., 2010), due to the relatively small thickness of the specimen (10 mm) compared to the other dimensions (typically 200 x 200 mm^2). However, recent experimental measurements indicate that a three-dimensional stress state may develop in the interior during dynamic rupture propagation.

Experimental measurements of the pressure c_p and shear c_s wave speeds, performed by tracking wave fronts in photoelastic fringe maps obtained during rupture propagation in such plates, reveal that the wave speed ratio is $c_p/c_s = 2$ (Mello et al., 2010, 2016), suggesting conditions close to plane strain even for specimens of 10 mm thickness (and other dimensions 20 times larger than the thickness). Photoelastic fringe patterns are produced in transmission mode, i.e. shining a laser beam from one side of a specimen and collecting it from the other, and are based on the change of an optical property, the refraction index of bi-refringent materials such as Homalite-100, while being mechanically deformed. As a result, these measurements carry information about the state of stress in the interior of the specimen. The fringe patterns obtained from photoelasticity are related to the maximum shear stress and do not provide information about the individual stress components. Nonetheless, the ratio of pressure to shear wave speed is a useful piece of information as it is related to the state of stress in the interior of the specimen. The wave speed ratio is a function of the Poisson's ratio ν of the solid, and it is given by $c_p/c_s = \sqrt{2(1-\nu)/(1-2\nu)}$ for plane-strain conditions, and by $c_p/c_s = \sqrt{2/(1-\nu)}$ for plane-stress conditions, respectively. Using the Poisson's ratio of Homalite-100, $\nu = 0.35$, yields a c_p/c_s ratio of 2.08 and 1.75, for plane-strain and plane-stress conditions, respectively. Hence, the experimental measurement of $c_p/c_s = 2$ would suggest that plane strain conditions prevail.

The dynamic ruptures studied here replicate the experimental configuration of Rubino et al. (2019, 2020) with a pre-stress level such as to produce intersonic ruptures. Intersonic, or supershear, ruptures are ruptures propagating at speeds exceeding the shear wave speed of the material but less than the pressure wave speed. Supershear rupture propagation was initially surmised based on theoretical and numerical analysis (Burridge, 1973; Andrews, 1976), it was later discovered in the laboratory (Rosakis et al., 1999; Rubinstein et al., 2004; Xia et al., 2004), and was subsequently inferred for crustal earthquakes (Bouchon et al., 2001; Ellsworth et al., 2004). Here we focus on the stress field associated with supershear rupture propagation along the frictional interface of plates with various thicknesses. The paper is organized as follows. First, we detail the finite element model, we describe the

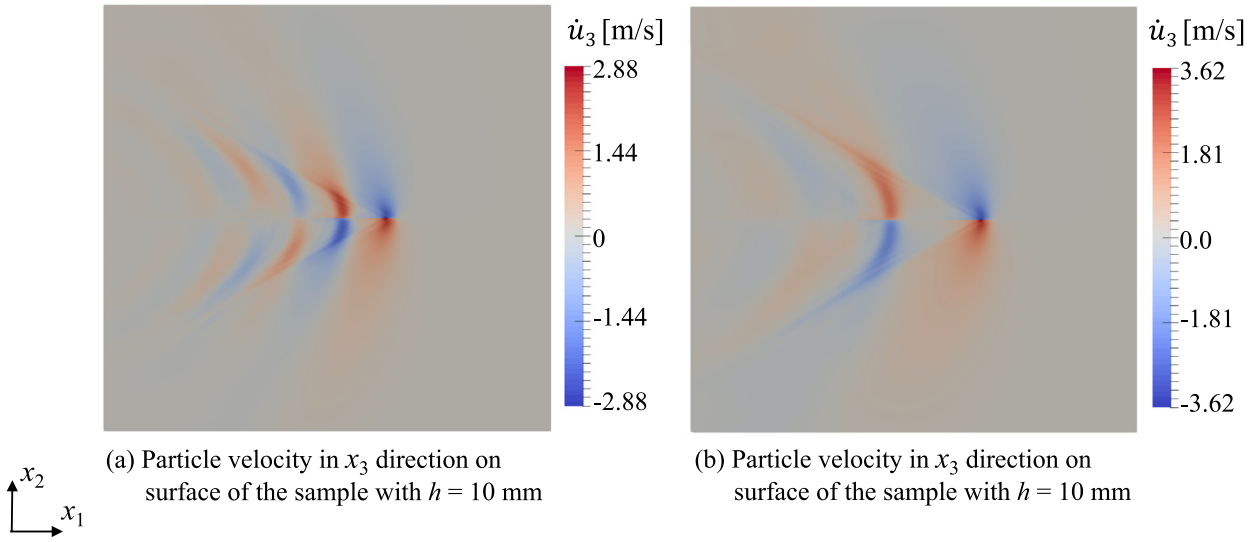

(a) Particle velocity in x_3 direction on surface of the sample with $h = 10$ mm

(b) Particle velocity in x_3 direction on surface of the sample with $h = 10$ mm

Fig. 4. Snapshots of the out-of-plane particle velocity field $\dot{u}_3$ on the free-surface ($x_3 = h/2$) during rupture propagation at $t = 54$ μs for a plate thickness h of (a) 10 mm and (b) 20 mm. The out-of-plane velocity field has an anti-symmetric structure and is characterized by lobes of alternating sign. The ranges of in-plane axes in the maps are $80 < x_1 < 227$ mm and $-70 < x_2 < 70$ mm.

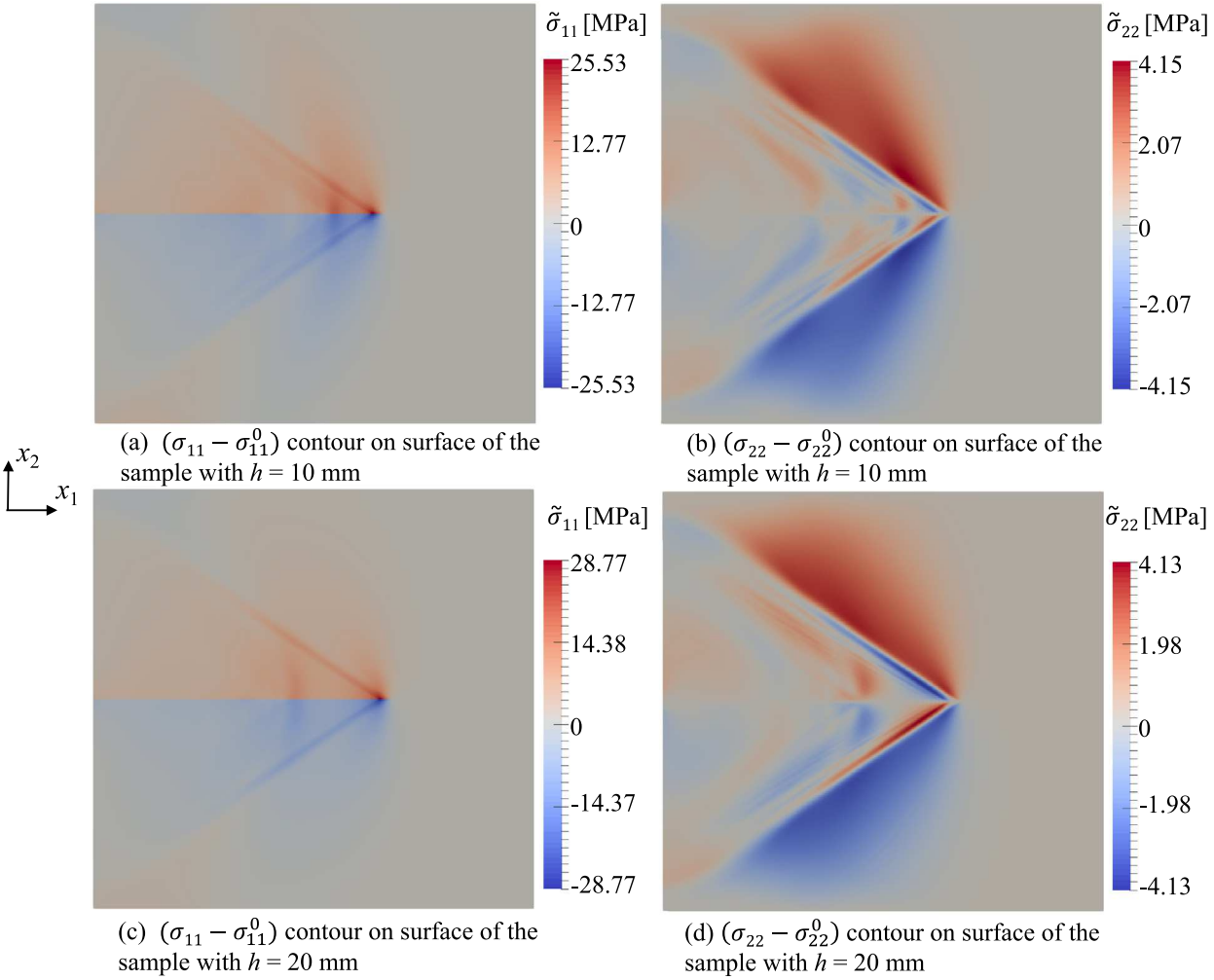

(a) $(\sigma_{11} - \sigma_{11}^0)$ contour on surface of the sample with $h = 10$ mm

(b) $(\sigma_{22} - \sigma_{22}^0)$ contour on surface of the sample with $h = 10$ mm

(c) $(\sigma_{11} - \sigma_{11}^0)$ contour on surface of the sample with $h = 20$ mm

(d) $(\sigma_{22} - \sigma_{22}^0)$ contour on surface of the sample with $h = 20$ mm

Fig. 5. Maps of the in-plane stress changes in the x_1 (left) and x_2 (right) directions on the free-surface ($x_3 = h/2$), at $t = 54$ μs, for the plates of thickness $h = 10$ mm (a, b) and $h = 20$ mm (c, d). The stress changes are defined with respect to the pre-stress levels before rupture arrival as: $\tilde{\sigma}_{11} = \sigma_{11} - \sigma_{11}^0$ and $\tilde{\sigma}_{22} = \sigma_{22} - \sigma_{22}^0$ in the interface-parallel (x_1) and interface-normal (x_2) directions, respectively. The maps are given in a region around the rupture tip, with in-plane axes range $80 < x_1 < 227$ mm and $-70 < x_2 < 70$ mm. The in-plane stress fields are related to the corresponding in-plane velocity fields and display similar features associated with the formation of shear Mach cones.

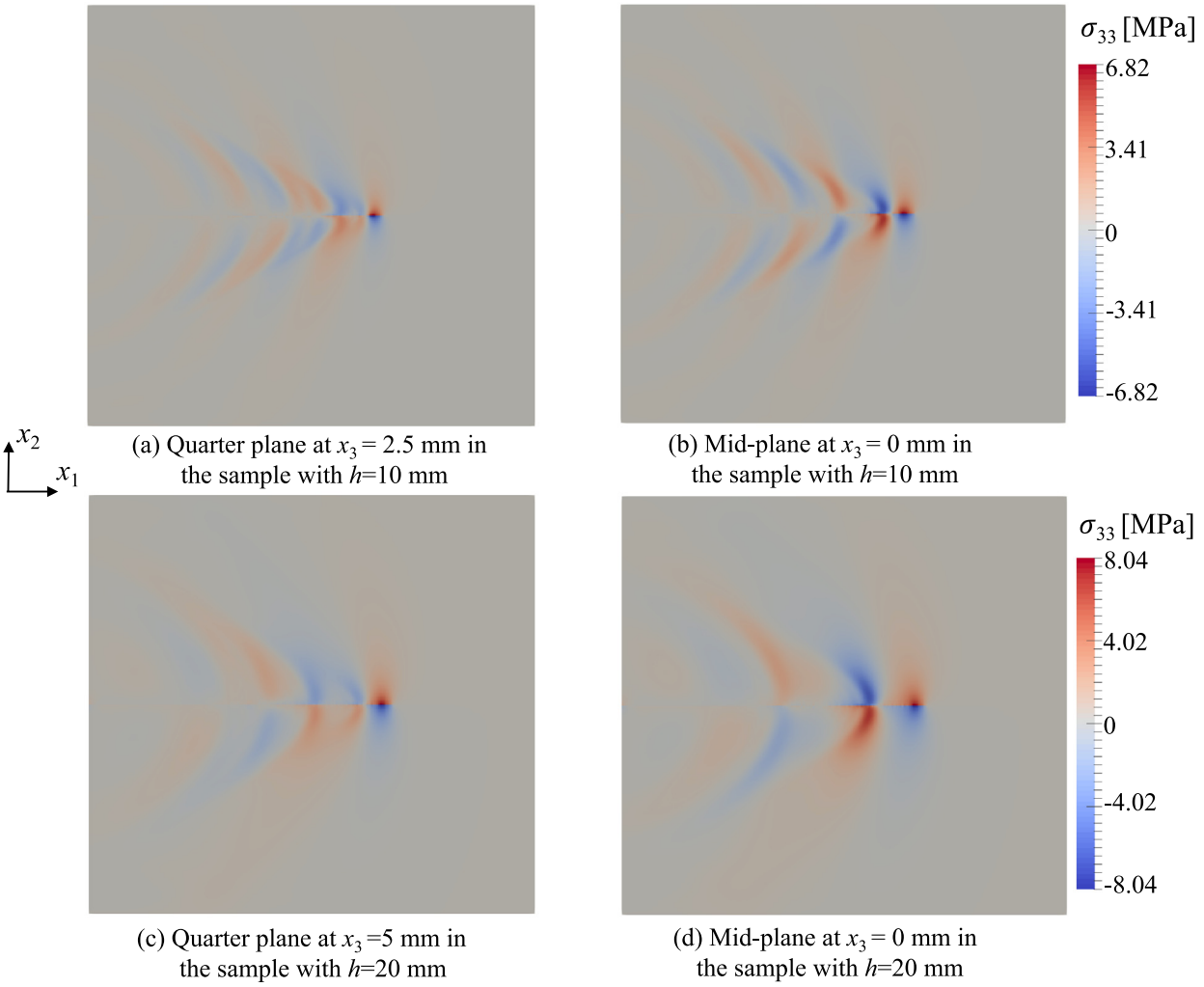

Fig. 6. Maps of the out-of-plane stress σ_{33} on the quarter ($x_3 = h/4$) and middle planes ($x_3 = 0$) at $t = 54$ μs, for the $h = 10$ mm (a, b) and $h = 20$ mm (c, d) thick plates. The plot is produced for a portion of the finite element model close to the rupture tip, such that $80 < x_1 < 227$ mm and $-70 < x_2 < 70$ mm.

in-plane and out-of-plane particle velocity fields on the outer surface, the in-plane stress components on the free-surface and the out-of plane stress in the interior of the specimen, for plates of two different thicknesses. Then, we analyze the particle velocities and shear stress components on the interface clarifying the kinematics as well as the deformation mode of dynamic shear ruptures through the specimen's thickness. Finally, we analyze the out-of-plane stress and the degree of stress three-dimensionality on the interface plane. This analysis shows the rapid development of a three-dimensional state of stress with the rupture arrival. The stress state approximates a state of plane-strain in the stress change components at the rupture front and has a complex pattern behind the rupture tip.

2. Finite element analysis of dynamic shear ruptures

2.1. Finite element modeling of the experimental ruptures

Dynamic ruptures along the interface of plates of various thicknesses are simulated numerically using a finite element model, inspired by the experimental setup described by Rubino et al. (2017). Two solid blocks of length $L = 227$ mm, height $H = 70$ mm, and thickness h are in contact along the $L \times h$ surface, as shown in Fig. 1b. Two different thicknesses $h = 10$ and 20 mm are used to investigate the effect of h in developing the out-of-plane stress. The reference systems has axes x_1 and x_2 in the interface-parallel and interface-normal directions respectively, and x_3 axis denoting the out-of-plane direction. The origin of the reference system is located at the intersection of the interface plane, and the two other midplanes, such that the two larger free-surfaces are located at $x_3 = \pm h/2$. The stress boundary conditions applied on the solids are computed as: $\sigma^0_{11} = -P\sin^2(\alpha)$; $\sigma^0_{22} = -P\cos^2(\alpha)$; and $\tau^0_{12} = -P\sin(\alpha)\sin(\alpha)$. Using the values of $P = 23$ MPa and $\alpha = 29$, the applied stresses are calculated as: $\sigma^0_{11} = -5.4$ MPa; $\sigma^0_{22} = -17.59$ MPa; $\tau^0_{12} = -9.75$ MPa. The superscripts denote the prestresses applied on the interface before rupture nucleation takes place. In the model we use the effective linear–elastic properties of Homalite-100, with a Young's modulus $E = 5.3$ GPa, Poisson's ratio $\nu = 0.35$, and mass density $\rho = 1200$ kg/m^3 (Rubino et al., 2019). The solids are discretized with uniform structured linear hexahedral elements of 0.45 mm edge length, which results in 500 elements along x_1 axis. Explicit dynamic time integration is employed to perform the finite element simulations. In each computational time step, a node-to-node contact algorithm is enforced on the interface between the two blocks, in which the contact forces required to prevent interpenetration is computed based on the nodal displacements perpendicular to the contact plane. In addition, for every node pair on the interface, frictional forces are calculated using the computed contact forces and the friction coefficient at that nodal position. The friction coefficient, in turn, is computed as a function of slip as described below in this section. Further details of the finite element modeling of contact and frictional interfaces is reported in Rezakhani et al. (2020). The numerical models described here are performed using the parallel open-source finite element library Akant, which can accessed at https://akantu.ch/.

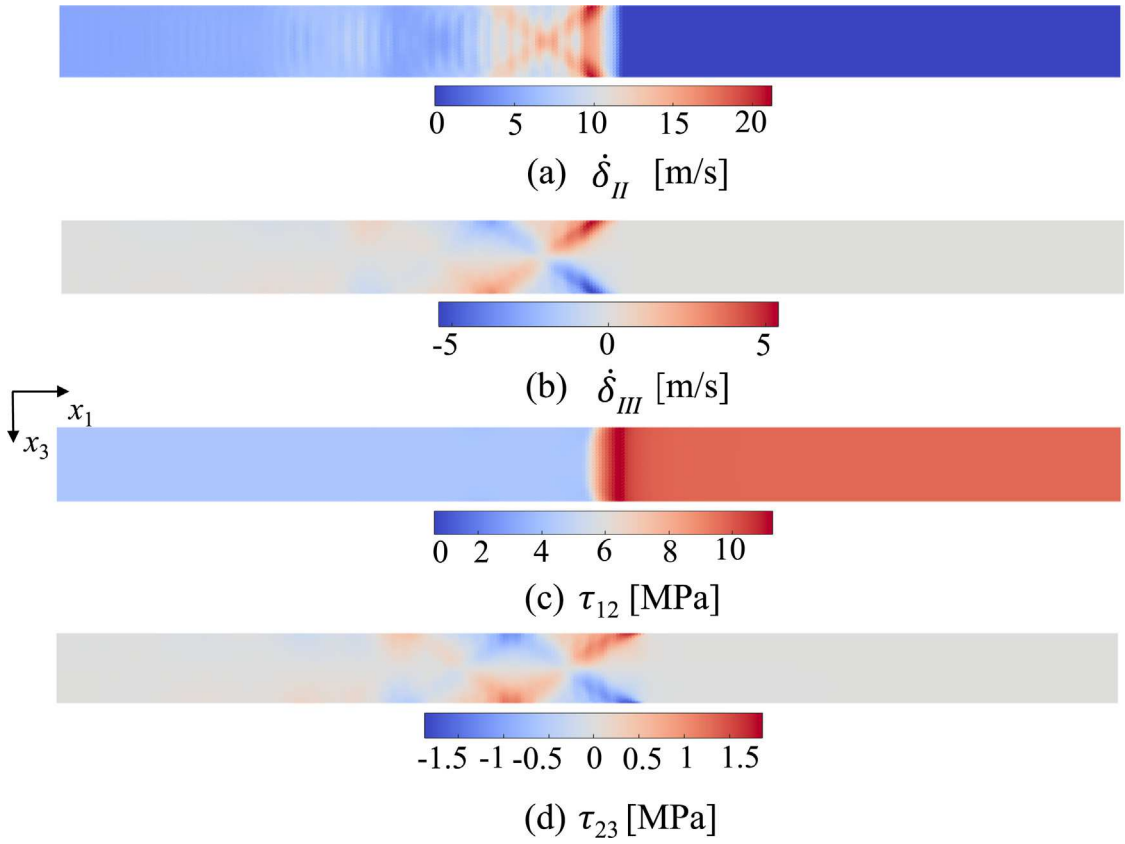

Fig. 7. Slip rates and shear stresses for the specimens of thickness $h = 10$ mm. (a) In plane and (b) out of plane slip rates. (c) In-plane and (d) out-of-plane shear stress components along the interface. The slip rates and shear stresses are plotted at time $t = 45$ μs after rupture nucleation.

In order to mimic the experimental rupture nucleation procedure (Lu et al., 2009, 2010; Rubino et al., 2017, 2019), the effects of the localized pressure increase is mimicked by a sudden reduction in the normal stress over a small region of the interface, the nucleation zone, and is then increased to its initial value. In the finite element simulations, the nucleation zone is considered as a rectangular patch with its center placed at $x_1 = 70$ mm and dimensions of $h \times 15$ mm, which results in its edge along x_1 axis over $62.5 < x_1 < 77.5$ mm. The evolution of the normal stress over the nucleation zone follows:

$$\sigma_{22}(t) = \begin{cases} \sigma_{22}^0 - \Delta P \cos\left(\frac{\pi}{2} - \frac{\pi t}{2t_0}\right) & \text{if } t < t_0 \\ \sigma_{22}^0 - \Delta P & \text{if } t_0 < t < t_0 + T_0 \\ \sigma_{22}^0 - \Delta P \cos\left(\frac{\pi t^*}{2t_0}\right) & \text{if } t_0 + T_0 < t < 2t_0 + T_0 \\ \sigma_{22}^0 & \text{if } t > 2t_0 + T_0 \end{cases} \quad (1)$$

in which t is time; ΔP is the amount of pressure increase; t_0 is the duration of pressure variation phase; T_0 is the duration, over which the reduced normal pressure is maintained; and $t^* = t - t_0 - T_0$. Using $\Delta P = 15$ MPa; $t_0 = 10$ μs; and $T_0 = 30$ μs, variation of σ_{22} over the nucleation zone with respect to time is plotted in Fig. 2a. As a result of the normal stress reduction over the nucleation zone described above, the applied shear stress on the interface overcomes the frictional strength leading to rupture propagation. Once nucleated, dynamic ruptures propagate bilaterally and symmetrically along the x_1 axis in the numerical simulations, similarly to the experimental ruptures. For the sake of clarity, we present the velocity and stress fields associated with the portion of the rupture propagating in the positive x_1 axis. The length scale over which the pressure perturbation occurs is chosen to roughly match the experimentally observed soot size, left in the wake of the wire burst. All other details describing the initiation procedure in the finite element simulation, including the amount of the pressure increase ΔP, and its time duration T_0, are chosen in order to produce supershear ruptures, as observed in the experiments under the same level of applied loading.

Dynamic rupture propagation along the frictional interface is controlled by the evolution of the friction coefficient with slip and slip rate. In the FE model presented here, we implement a commonly used friction law, the slip-weakening formulation of friction (Kanamori and Rivera, 2006; Liu and Lapusta, 2008; Dedontney et al., 2008; Templeton et al., 2009). In this formulation, the friction coefficient f decreases linearly with slip δ from the static value f_s to the dynamic level f_d, over a length scale D_c, according to:

$$f = \begin{cases} f_s - \frac{\delta}{D_c}(f_s - f_d) & \text{if } (\delta < D_c) \\ f_d & \text{if } (\delta > D_c) \end{cases} \quad (2)$$

In the linear slip-weakening law f_s, f_d, and D_c are considered as material constants. At the same time, experiments have shown that these parameters, and in turn friction evolution, are actually controlled by slip rate and its history, as well other effects (Dieterich, 2007; Ben-David et al., 2010; Goldsby and Tullis, 2011; Di Toro et al., 2011; Ikari et al., 2011; Brown and Fialko, 2012; Rubino et al., 2017). Linear slip-weakening can be used, nonetheless, as an effective law with f_s, f_d and D_c as effective parameters (Rubino et al., 2017; Rosakis et al., 2020), which are calibrated using the experimental measurements as illustrated in Fig. 2b. The effective friction parameters employed in the simulations are: $f_s = 0.64$; $f_d = 0.24$, and $D_c = 25$ μm (Fig. 2b), consistent with the experimental measurements presented by Rubino et al. (2017) for dynamic ruptures produced with the same level of applied prestress.

2.2. Analysis of the finite element results

Two key quantities in the study of shear ruptures are the displacement jump across the interface, the slip δ, and its rate $\dot{\delta}$. Slip is

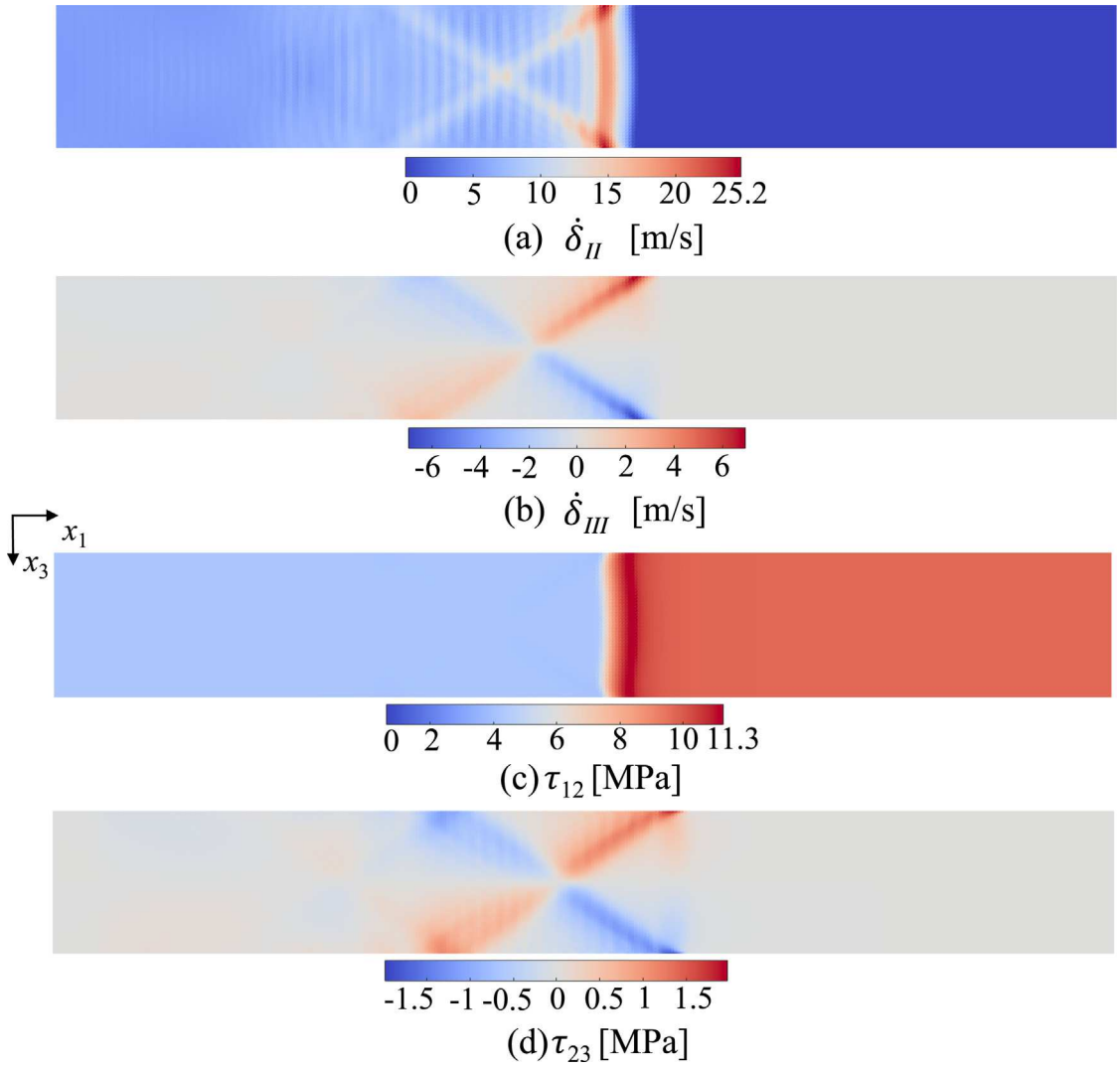

Fig. 8. Slip rates and shear stresses for the specimens of thickness $h = 20$ mm. (a) In plane and (b) out of plane slip rates. (c) In-plane and (d) out-of-plane shear stress components along the interface. The slip rates and shear stresses are plotted at time $t = 45$ μs after rupture nucleation.

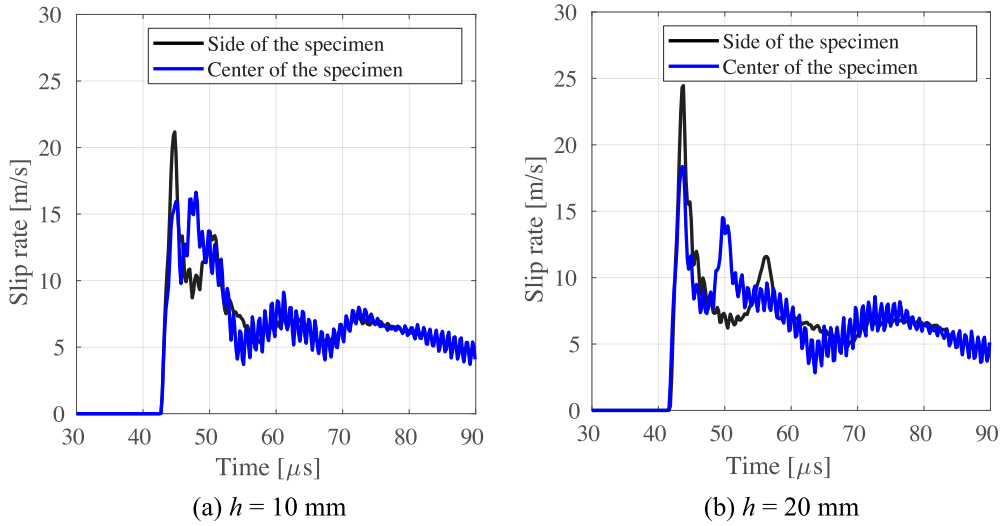

Fig. 9. Slip rate time history in the interface-parallel direction measured at $x_1 = 82$ mm from the nucleation site for a plate thickness of (a) 10 mm and (b) 20 mm. In each case, the slip rate is measured on the free-surface ($x_3 = h/2$), and on the midplane ($x_3 = 0$). These plots show the presence of two peaks, whose spatial and temporal spacing increases with the plate thickness. The double-peak feature is due to the formation of shear Mach cones through the thickness of the specimen, as shown by Figs. 7a and 8a, and as discussed in the text.

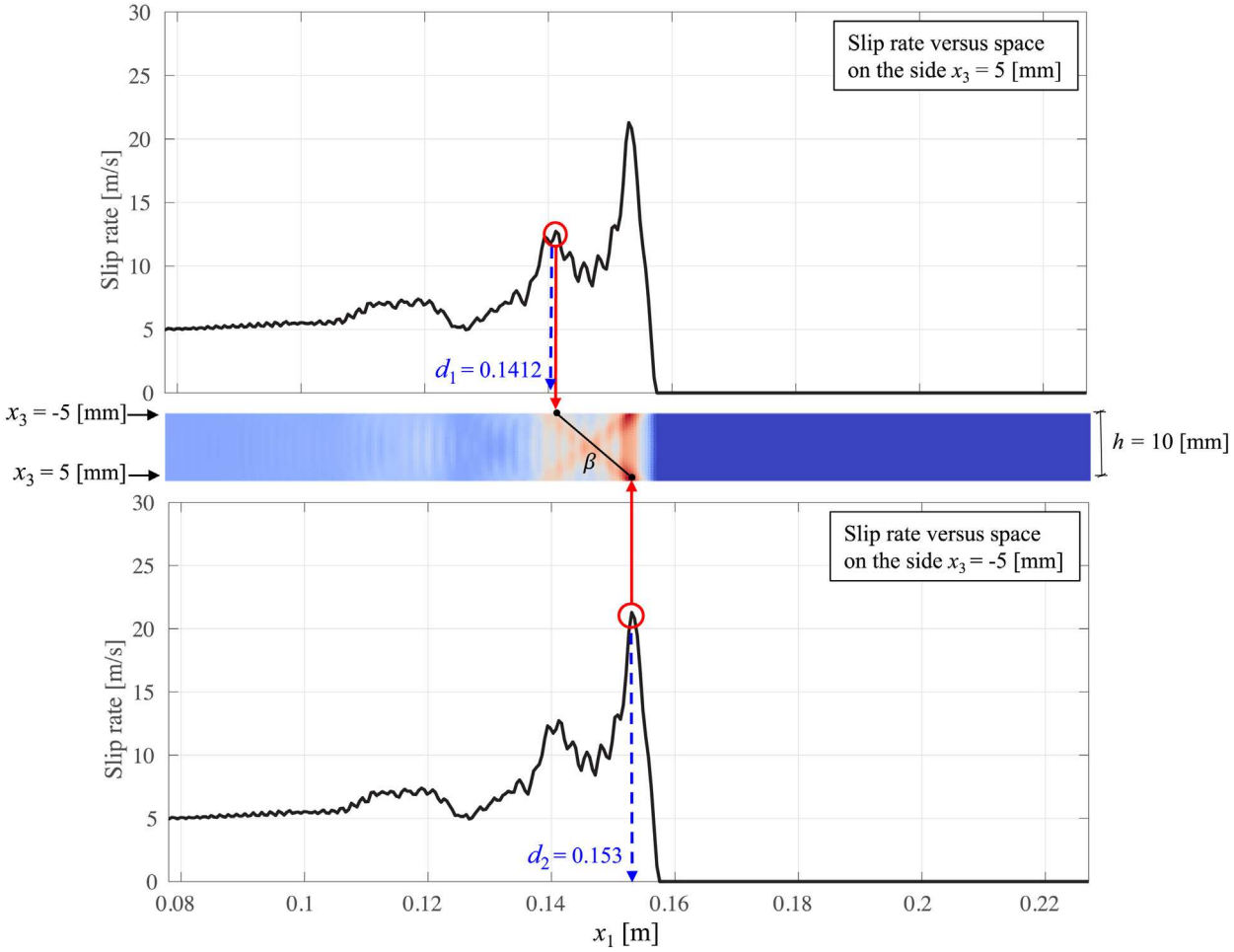

Fig. 10. Slip rate $\dot{\delta}_{II}$ map for the plate of thickness $h = 10$ mm at $t = 45$ μs together with plots of $\dot{\delta}_{II}$ vs. x_1 plotted at the free-surfaces $x_3 = -h/2$ (top) and $x_3 = h/2$ (bottom).

computed along the interface plane $x_2 = 0$ in the x_1 and x_3 directions as the difference of the in-plane u_1 and out-of-plane u_3 displacement components of adjacent nodes immediately above and below the interface, e.g. $\delta_{II}(x_1, x_3) = u_1^-(x_1, x_3) - u_1^+(x_1, x_3)$, and $\delta_{III}(x_1, x_3) = u_3^-(x_1, x_3) - u_3^+(x_1, x_3)$, for mode II and mode III motions respectively. The notation u^+ and u^- refers to the displacement components of the nodes immediately above and below the interface at $x_2 = 0$, respectively. The in-plane $\dot{\delta}_{II}(x_1, x_3)$, and $\dot{\delta}_{III}(x_1, x_3)$ slip rate components are computed as the time derivatives of the corresponding slip components.

Rupture speed is computed by tracking the rupture tip of the propagating ruptures along the interface. The rupture tip position as a function of time is identified by analyzing the in-plane slip rate component $\delta_{II}(x_1, x_3)$ vs. position on the interface $x_2 = 0$. A threshold of 0.5 m/s is set on the slip rate to determine rupture arrival. Slip rate curves are considered with a temporal interval of 5 μs. Rupture speed is then obtained as the time derivative of the rupture tip position time function.

3. Three dimensional finite element simulations describing the state of stress in the interior of the specimen

3.1. In-plane and out-of-plane particle velocity fields

In this section we analyze the patterns of the in-plane (x_1 - x_2) and out-of-plane (x_3) particle velocities. The components in the x_1 (interface-parallel) and x_2 (interface-normal) directions of particle velocity obtained from the FE simulations display an anti-symmetric and symmetric pattern, respectively (Fig. 3), as expected from analytical models of dynamic shear ruptures in mode II (Freund, 1998; Mello et al., 2016), and consistent with recent full-field experimental measurements (Rosakis et al., 2020; Rubino et al., 2020). The particle velocities are also characterized by sharp discontinuities associated with the formation of shear Mach cones (Fig. 3), indicating the supershear nature of the dynamic rupture. Supershear propagation is due to the relatively high level of applied pre-stress, in line with theoretical predictions and experimental findings (Burridge, 1973; Andrews, 1976; Mello et al., 2010, 2016; Rubino et al., 2017). Tracking the rupture tip along the interface, as explained in Section 2.2, confirms the supershear nature of the ruptures presented here. This analysis results in rupture speeds of $V_r = 2.23$ km/s and $V_r = 2.31$ for the two cases of $h = 10$ mm and 20 mm, respectively, which are greater than the shear wave speed of Homalite-100, $c_s = 1.28$ km/s.

The out-of-plane velocity field is characterized by an anti-symmetric field, also displaying shock features associated with the shear Mach cone (Fig. 4), though less prominent than for the in-plane components. This field is the time derivative of the out-of-plane displacement u_3. Note that the out-of-plane displacement u_3 and velocity $\dot{u}_3$ depend on the out-of-plane strain. The displacement field u_3 on the free-surfaces is obtained from the out-of-plane strain, integrated over the half thickness. For example, on the free surface $x_3 = h/2$, the out-of-plane displacement is given by: $u_3(x_1, x_2) = \int_0^{h/2} \epsilon_{33}(x_1, x_2, x_3)\, dx_3$, where $\epsilon_{33} = -\nu/E\,(\sigma_{11} + \sigma_{22}) + 1/E\,\sigma_{33}$. Under plane-stress conditions, $\sigma_{33} = 0$ through the thickness and the out-of-plane displacement may be simply computed from the in-plane stress components: $u_3(x_1, x_2) = -\nu h/2E(\sigma_{11}+\sigma_{22})$ on the free-surface. This observation has an important practical implication for the experimental measurements. Under plane-stress conditions, the out-of-plane displacement may be obtained from

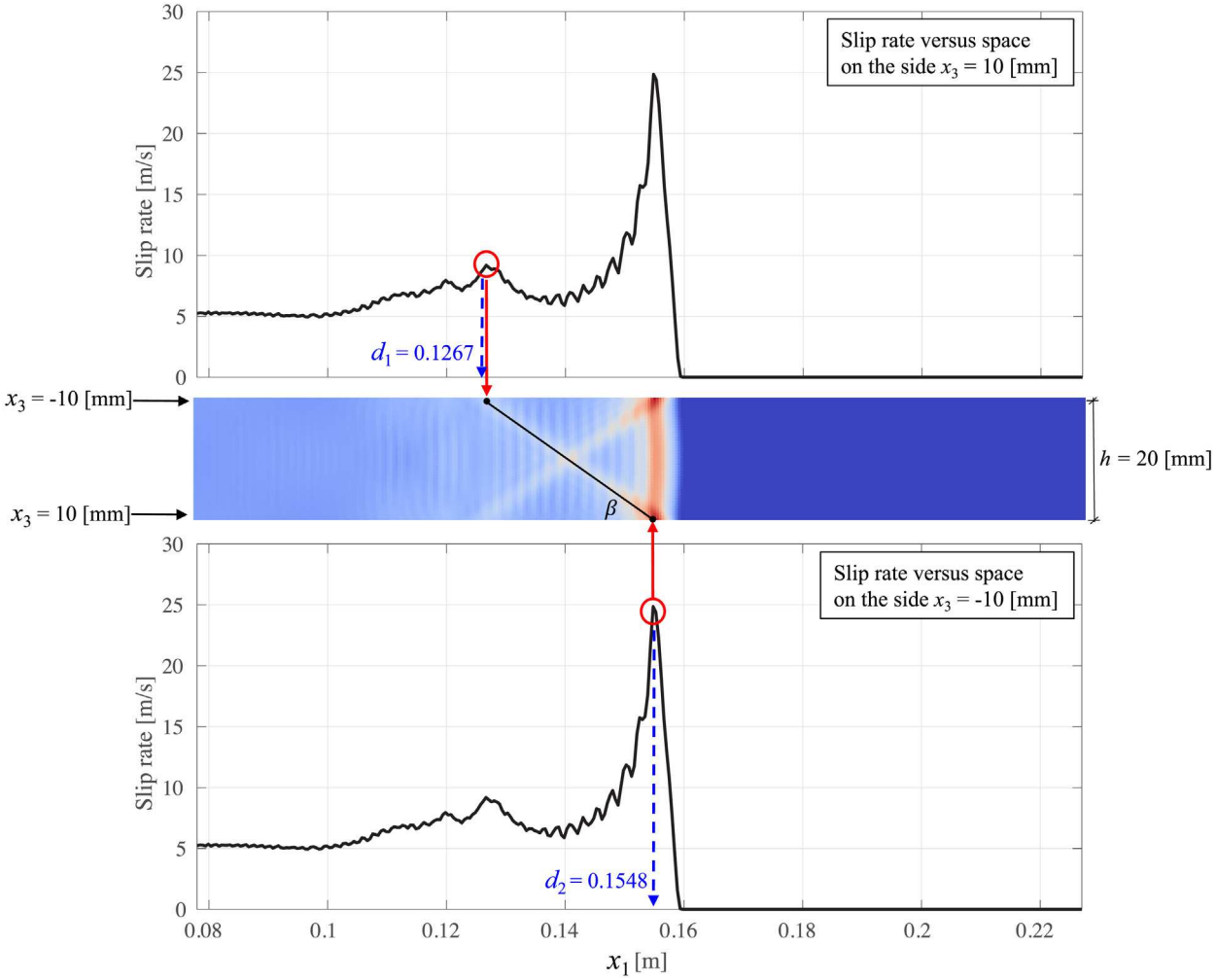

Fig. 11. Slip rate $\dot{\delta}_{II}$ map for the plate of thickness $h = 20$ mm at $t = 45$ μs together with plots of $\dot{\delta}_{II}$ vs. x_1 plotted at the free-surfaces $x_3 = -h/2$ (top) and $x_3 = h/2$ (bottom).

in-plane measurements without the use of complex diagnostics involved for stereoscopic measurements of the out-of-plane displacements. However, as it will be shown shortly, dynamic rupture propagation results in a three-dimensional stress state so that fully 3D FE simulations are needed to correctly reproduce the displacement fields. Similarly, the out-of-plane displacement component has to be experimentally measured independently from the in-plane components, using a 3D measurement approach. The out-of-plane velocity field is also characterized by lobes of different polarity, which will be interpreted in the next section.

3.2. Generation of out-of-plane stress in the interior of the specimen

To better understand the effect of dynamic rupture propagation on the stress pattern, we plot the in-plane stress changes over the applied stress level before rupture arrival, namely $\tilde{\sigma}_{11} = \sigma_{11} - \sigma^0_{11}$ and $\tilde{\sigma}_{22} = \sigma_{22} - \sigma^0_{22}$ in the interface-parallel and interface-normal direction, respectively. Similarly to the particle velocity fields, the in-plane stress components display discontinuity features associated to the supershear propagation of the dynamic rupture (Fig. 5). The interface-parallel component displays two lobes associated with the dilatational field, radiating from the rupture tip with the upper plate in tension and the lower plate in compression. The interface-normal stress change has corresponding tensional and compressional lobes radiating from the rupture tip, followed by lobes of alternating polarity, behind the rupture tip.

Before rupture arrival, plane stress conditions dominate over the entire specimen, with $\sigma_{33} = \sigma_{13} = \sigma_{23} = 0$, and $\partial\sigma_{i3}/\partial x_3 = 0$, with i = 1, 2, 3. As the rupture arrives, it perturbs the state of stress. Full-field maps of the out-of-plane stress reveal the development of nonzero σ_{33} in the bulk of the plate (Fig. 6), while maintaining $\sigma_{33} = 0$ on the free surfaces. The three-dimensional stress field is concentrated in the near-rupture tip, with plane-stress conditions still governing in the far field. The maps of out-of-plane stress, produced on the midplane ($x_3 = 0$) and on the quarter plane ($x_3 = h/4$), for both specimen thicknesses, indicate that σ_{33} intensifies as it reaches the midplane.

3.3. Slip rate and shear stress fields over the interface plane

In order to understand how slip rate and shear stress vary through the thickness, we plot the slip rates and shear stress components along the interface plane $x_2 = 0$, for the two cases of plate thickness $h =$ 10 mm and 20 mm, in Figs. 7 and 8, respectively. The full-field maps across the specimen's thickness of both components of slip rate, $\dot{\delta}_{II}$ and $\dot{\delta}_{III}$, and the out-of-plane shear stress τ_{23} are characterized by sharp features across the thickness of the specimen and intersecting at the midplane. In particular, the in-plane component of slip rate $\dot{\delta}_{II} = \dot{u}_2^- - \dot{u}_2^+$ exhibits a pronounced peak immediately behind the rupture tip, followed by a second peak (Figs. 7a and 8a). This feature becomes clearer when plotting $\dot{\delta}_{II}(t)$ vs. t, on the free-surface ($x_3 = h/2$) and on the mid-plane ($x_3 = 0$) at a fixed location along the interface ($x_1 = 82$ mm) (Fig. 9). The spacing between the two peaks changes as a function of the coordinate x_3, with a maximum spacing on the

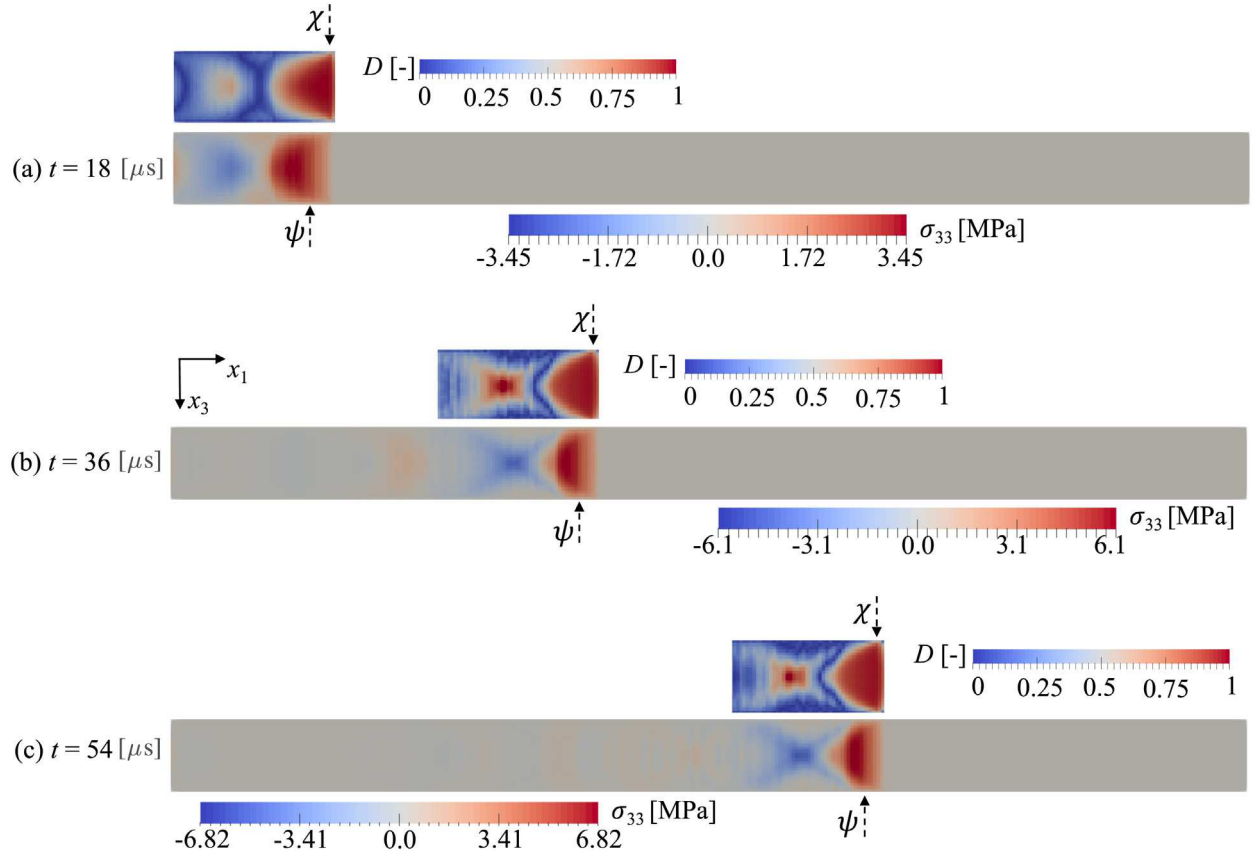

Fig. 12. Maps of the out of plane stress σ_{33} and degree of plane strain D on the interface plane $x_2 = 0^+$, on the first row of elements above the interface, at three time instants and for the plate of thickness $h = 10$ mm.

free-surface and minimum distance on the midplane, for each thickness. Since the two peaks are generated by the field structure shown in Figs. 7a and 8a, the specimen with larger thickness is also characterized by a wider spacing of the peaks.

The double-peak feature has also been observed experimentally on the outer surface, by means of laser velocimeter traces (Lu et al., 2010; Mello et al., 2010) or digital image correlation measurements (Rubino et al., 2017, 2019), and has been attributed to the formation of shear Mach cones in supershear ruptures through the thickness of the specimen (e.g. Mello et al. (2010), Rubino et al. (2017)). According to this idea, supershear ruptures propagating through thicker plates would display a larger spacing between interface-parallel velocity, and consequently slip rate, peaks. The increasing spacing of the particle velocity peaks with plate thickness was verified experimentally by performing particle velocity measurements on the outer surface, where measurements are possible, of plates of various thicknesses (Lu et al., 2010). On the other hand, the double-peak feature is not observed for sub-Rayleigh ruptures where Mach features are not formed (Rubino et al., 2020).

To verify that the observed structure, exhibited by the slip rate $\dot{\delta}_{II}$ through the thickness of the specimen, is actually due to the formation of a shear Mach cone, we check that the angle β formed by the slip rate feature with the specimen surface is consistent with the Mach cone relation $\sin(\beta) = c_s/V_r$. The angle β can be measured as: $\beta = \arctan(h/(d_2 - d_1))$, where d_1 and d_2 are the distances from the initiation site of the intersection of the Mach feature with the free surfaces at $x_1 = -h/2$ and $x_1 = h/2$, respectively (Figs. 10 and 11). This relation yields $\beta = 40.3°$ and $35.4°$, for the specimens of thickness $h = 10$ and 20 mm, respectively. Using the measured angle β and the shear wave speed c_s, we can compute the estimated rupture speed through the Mach cone relationship. The rupture propagation speeds associated with the measured angle β are $V_r = c_s/\sin(\beta) = 1.98$ km/s and 2.21 km/s, for the case of lower and higher thickness, respectively. These estimates are consistent (within 5%–10%) with the rupture speed obtained independently by tracking the rupture tip, as explained in Section 2.2, which gives $V_r = 2.23$ km/s and 2.31 km/s, for the two thicknesses, respectively. This analysis confirms that the sharp features displayed by the full-field maps of the slip rates and shear stress component τ_{23} are indeed due to the formation of two shear Mach cones, one on each side, where the rupture front intersects the free surfaces at $x_3 = \pm h/2$. These shear Mach cones are visible when monitoring the particle velocity on the free-surface $x_3 = \pm h/2$ (Fig. 3) and the slip rate features visualized in Figs. 7a and 8a are the generatrices of such cones resulting from the intersection of the Mach cone surface with the interface plane.

The through-thickness features of out-of-plane component of slip rate $\dot{\delta}_{III} = \dot{u}_3^- - \dot{u}_3^+$ and shear stress τ_{23} display alternate polarity (Figs. 7b–d and 8b–d, respectively). The development of out-of-plane slip rate $\dot{\delta}_{III}$ is explained by the anti-symmetric behavior of the out of-plane particle velocity $\dot{u}_3$ and displacement u_3 with respect to the interface plane, which in turn depend on the strain change of out-of-plane strain during rupture propagation $\tilde{\epsilon}_{33} = -\nu/E(\tilde{\sigma}_{11} + \tilde{\sigma}_{22}) + \nu/E\tilde{\sigma}_{33}$, as discussed in Section 3 (Fig. 4). Since the stress components $\tilde{\sigma}_{11}$ and $\tilde{\sigma}_{33}$ are anti-symmetric with respect to the interface, while $\tilde{\sigma}_{22}$=0 on the interface (Fig. 5), they result in the anti-symmetry of $\tilde{\epsilon}_{33}$ and hence generating the out-of-plane slip rate $\dot{\delta}_{III}$. This deformation mode also results in the out-of-plane shear strains ϵ_{23} and associated shear stresses τ_{23} (Figs. 7d and 8d).

Ahead of the rupture tip, the in-plane shear stress component τ_{12} along the interface plane is at a uniform level of 9.8 MPa, given by the applied level of pre-stress. As the rupture arrives, τ_{12} is characterized by an initial rapid increase over the pre-stress level, up to about 12 MPa,

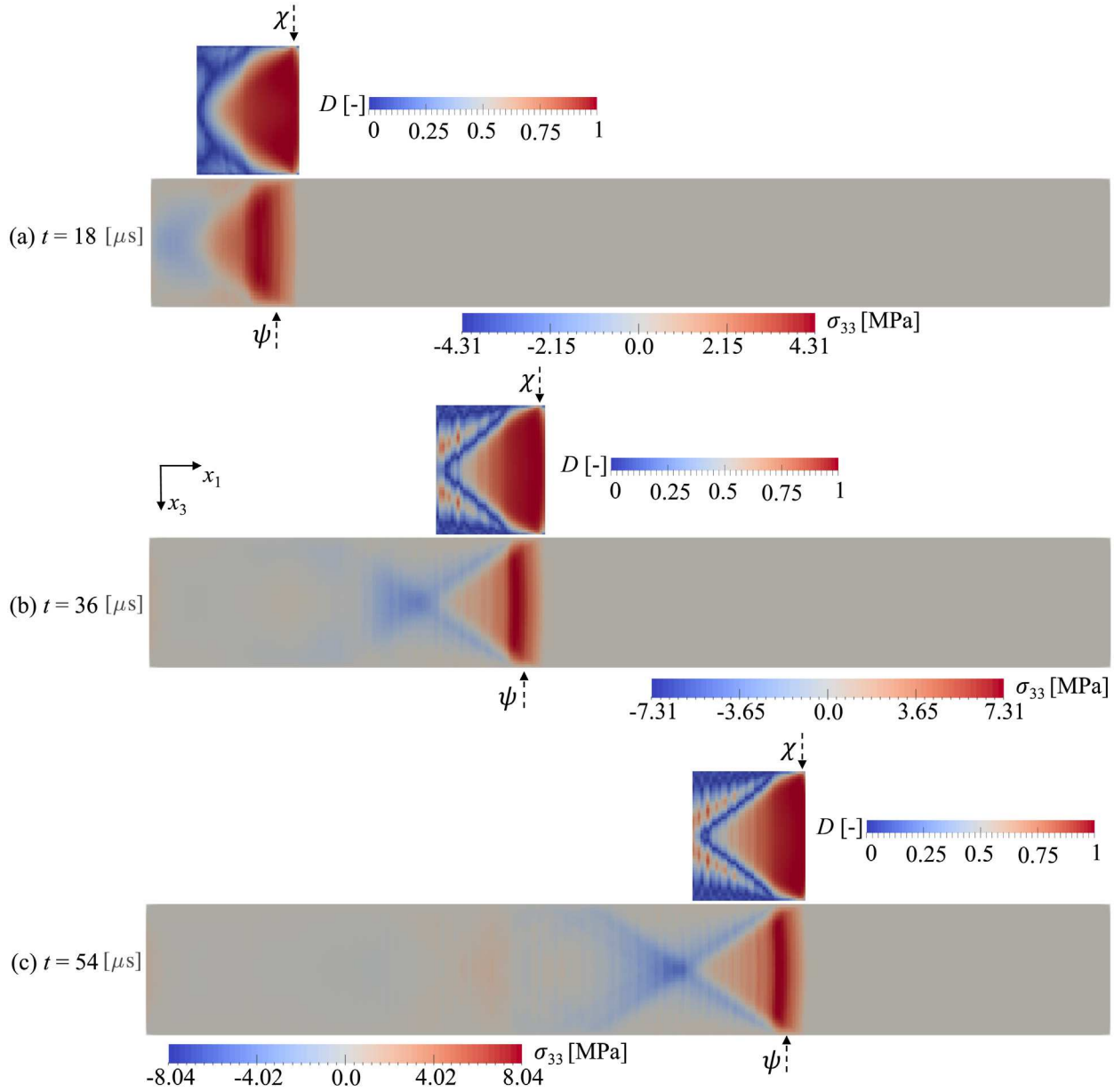

Fig. 13. Maps of the out of plane stress σ_{33} and degree of plane strain D on the interface plane $x_2 = 0^+$, on the first row of elements above the interface, at three time instants and for the plate of thickness $h = 20$ mm.

and by a subsequent drop to 4.5 MPa (Figs. 7c and 8c), consistent with experimental measurements on the outer surface (Rubino et al., 2017). Since the interface-normal stress σ_{22} is constant along the interface, the in-plane shear stress variations are directly linked to the friction evolution $f = \tau_{12}/\sigma_{22}$, observed experimentally (Rubino et al., 2017). Note that the through-thickness profiles of the in-plane slip rate and shear stress, which are associated with the rupture front, present a slight convexity towards the unruptured portion of the interface for most of the interface and a concavity in the proximity of the free-surfaces, at $x_3 = \pm h/2$. This shows that the rupture front is not planar but rather has the more complex geometry suggested by Figs. 7a–c and 8a–c.

3.4. Out-of-plane stress map over the interface plane

To understand how dynamic rupture propagation influences the out-of-plane stress component σ_{33}, and its transition from the free-surface condition $\sigma_{33} = 0$ at $x_3 = \pm h/2$ to nonzero values attained through the thickness, as revealed by Fig. 6, we map $\sigma_{33}(x_1, x_3)$ on the interface plane $x_2 = 0^+$ (Figs. 12 and 13). One quantity useful to monitor the state of stress is the degree of plane strain, defined as the ratio: $|\sigma_{33}/(\nu\,(\sigma_{11} + \sigma_{22}))|$. The degree of plane strain is a measure of the stress three-dimensionality in the proximity of the rupture tip. In plane-strain conditions, it is equal to 1 as $\sigma_{33} = -\nu\,(\sigma_{11} + \sigma_{22})$, and it is equal to zero in plane-stress conditions when $\sigma_{33} = 0$, or at the free surface. This ratio has been used in previous studies to explore stress three-dimensionality in mode I cracks (Rosakis et al., 1990; Tippur, 1990; Lee and Rosakis, 1993). In general, it can be shown that, using the superposition principle, the stress solution of a 3D problem can be decomposed in a 2D plane-strain problem and a remainder solution. Under symmetric loading conditions, such as those used in the crack problem of Rosakis et al. (1990), Tippur (1990), Lee and Rosakis (1993), the remainder solution becomes zero and the stress field in the near-tip region is given by the 2D plane strain solution. Since here we are interested in studying mode II rupture propagation along interfaces under (non-symmetric) pre-stressed conditions, we track the

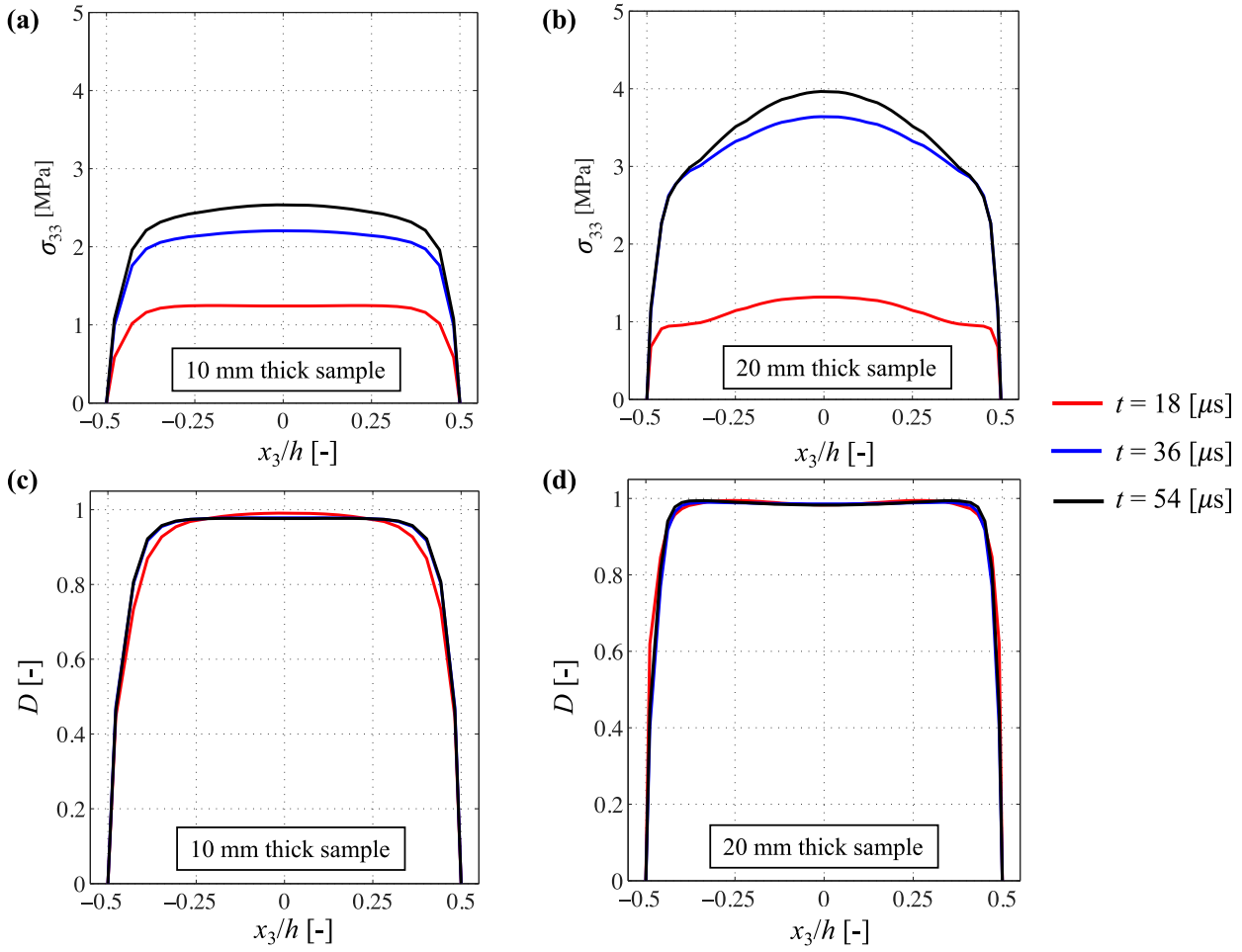

Fig. 14. Plots of the out-of-plane stress and ratio D across the thickness, at the cross-section χ shown in Figs. 12 and 13. σ_{33} versus x_3/h for (a) 10 mm and (b) 20 mm thick specimens at the three time instants presented in Figs. 12 and 13. These curves are plotted at the rupture front, where D reaches its maximum value. The stress ratio $D = |\sigma_{33}/(\nu \times (\tilde{\sigma}_{11} + \tilde{\sigma}_{22}))|$ is plotted vs. x_3/h along the same cross-sections for (c) 10 mm and (d) 20 mm thick samples. $\tilde{\sigma}_{11} = \sigma_{11} - \sigma^0_{11}$ and $\tilde{\sigma}_{22} = \sigma_{22} - \sigma^0_{22}$ are stress components subtracted by the far field applied stresses depicted in Fig. 1.

stress changes $\tilde{\sigma}_{ij} = \sigma_{ij} - \sigma^0_{ij}$, where σ^0_{ij} is the applied pre-stress. The degree of plane strain is then defined with respect to the stress changes as: $D = |\tilde{\sigma}_{33}/(\nu\,(\tilde{\sigma}_{11} + \tilde{\sigma}_{22}))|$. Note that $\tilde{\sigma}_{33} = \sigma_{33}$, as the initial loading configuration results in plane-stress conditions. The ratio D so defined is still a measure of the stress three-dimensionality in the proximity of the rupture tip. The condition $D = 1$, when $\tilde{\sigma}_{33} = -\nu(\tilde{\sigma}_{11}+\tilde{\sigma}_{22})$, indicates a plane-strain-like condition in the stress field $\tilde{\sigma}_{ij}$. On the other hand $D \to 0$ as $\tilde{\sigma}_{33}$ approaches zero at the free surface. However, D is not defined ahead of the rupture tip.

The maps of out-of-plane stress σ_{33} over the interface plane confirm plane-stress conditions in the specimen before rupture arrival (Figs. 12 and 13). The plots are given for the first row of elements immediately above the interface ($x_2 = 0^+$). As the dynamic rupture arrives, σ_{33} sharply deviates from plane-stress conditions, inducing a three dimensional state of stress in the bulk of the specimen, for both thicknesses considered. The out-of-plane stress becomes positive at the rupture tip with a maximum value at the midplane ($x_3 = 0$), and increasing as the rupture propagates along the interface. Snapshots of σ_{33} over the interface reveal how the out-of-plane increases from just shy of 4 MPa at $t = 18$ μs (Fig. 12a) to nearly 7 MPa, at $t = 54$ μs (Fig. 12c), in the case of the 10 mm thick specimen, and even larger values of σ_{33} are attained in the case of the 20 mm thick specimen. Meanwhile, as the out-of-plane stress σ_{33} increases, the stress ratio D also picks up and reaches the value of $D = 1$ at the midplane, indicating plane-strain conditions in the stress changes $\tilde{\sigma}_{ij}$. Behind the rupture tip, D is still positive but attests levels less than one, indicating a fully three-dimensional stress state, even with respect to the stress change.

Following the initial region of tensile (compressive) stresses, immediately above (below) the interface, the out-of-plane stress develops compressive (tensile) crisscrossing features, intersecting at the midplane (Figs. 12 and 13). These features are inclined by an angle $\beta = \arcsin c_s/V_r$ with respect to the free-surface, similarly to what observed with the slip rate features (Figs. 10 and 11). As the rupture propagates along the interface, these sharp features intensify and extend almost all the way to the interface. A selection of snapshots of $\sigma_{33}(x_1, x_3)$ on the plane $x_3 = 0+$ reveals that the pattern of negative σ_{33} has not developed yet at the early stages of rupture propagation time ($t = 18$ μs) (Figs. 12a and 13a, for the two thicknesses respectively). The pattern starts developing at $t = 36$ μs (Figs. 12b and 13b) and intensifies as the later stages of rupture propagation, showing higher magnitudes at $t = 54$ μs (Figs. 12c and 13c). The crisscrossing pattern is most evident just after the tensile region behind the rupture tip, but a similar, repeating pattern is present though attenuating further behind, as suggested by Fig. 6. Note that the $\sigma_{33}(x_1, x_3)$ on planes $x_3 = \text{const}$ has an anti-symmetric pattern with respect to the interface, so the polarities just described for $\sigma_{33}(x_1, x_3)$ immediately above the interface, have opposite signs below the interface. Snapshots tracking the evolution of out-of-plane stress on planes during rupture propagation show that plane stress conditions are recovered after the rupture swipes through the interface (Figs. 12 and 13). Eventually, plane-stress conditions are recovered at a distance behind the rupture tip equal to several plate

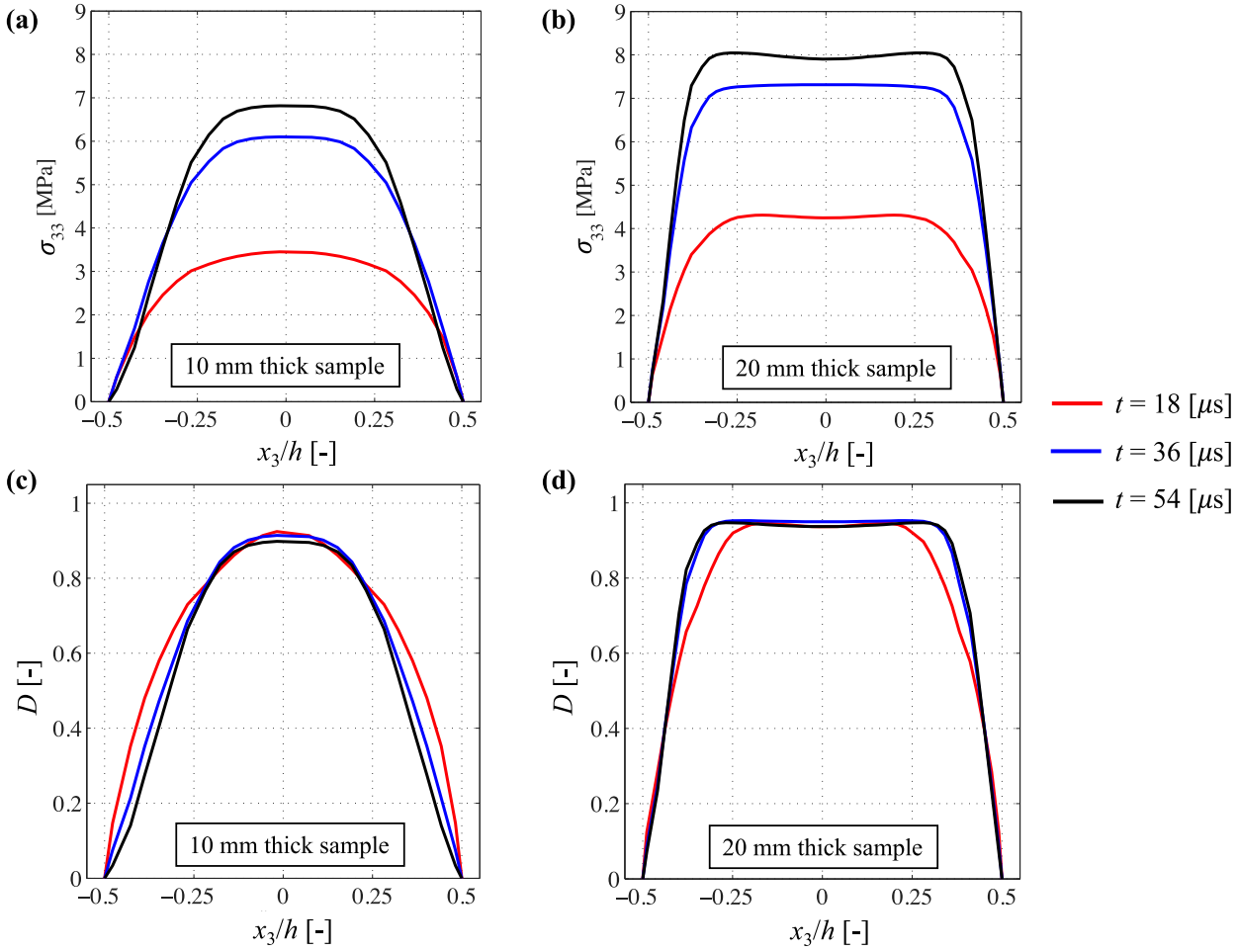

Fig. 15. Plots of the out-of-plane stress and ratio D across the thickness, at the cross-section ψ shown in Figs. 12 and 13. σ_{33} versus x_3/h for (a) 10 mm and (b) 20 mm thick specimens at the three time instants presented in Figs. 12 and 13. These curves are plotted just behind the rupture front, where σ_{33} reaches its maximum value. The stress ratio $D = |\sigma_{33}/(\nu \times (\tilde{\sigma}_{11} + \tilde{\sigma}_{22}))|$ vs. x_3/h is plotted at the same locations for (c) 10 mm and (d) 20 mm thick samples. $\tilde{\sigma}_{11} = \sigma_{11} - \sigma^0_{11}$ and $\tilde{\sigma}_{22} = \sigma_{22} - \sigma^0_{22}$ are stress components subtracted by the far field applied stresses depicted in Fig. 1.

thicknesses. However, most of the 3D effects are attenuated after a distance equal to twice the plate thickness. These simulations indicate a more marked three-dimensional effect of dynamic cracks on the stress field compared to static cracks, where plane stress conditions are recovered at a distance of half the thickness from crack tip (e.g. Lee and Rosakis, 1993).

To further understand how quickly the out-of-plane stress deviates from the free-surface condition, and how the state of stress changes in the bulk of the specimen during dynamic rupture propagation, we plot σ_{33} and the ratio D vs. x_3/h (Figs. 14 and 15), at the two cross-sections χ and ψ shown in Figs. 12 and 13, respectively. The two cross-sections denoted by the planes χ and ψ are selected because they correspond to the locations where D and σ_{33} reach their maximum, respectively. The plane χ denotes the rupture front, while the plane ψ is a short distance behind it. The plots of Figs. 14 and 15 show that both the out-of-plane stress and ratio D rapidly deviate from the free-surface condition.

At the rupture tip, the out-of-plane stress reaches a peak that is more pronounced in the case of $h = 20$ mm, and flatter for the case of $h = 10$ mm. The peak becomes higher as the rupture grows, at larger level of t, as previously noted. Most importantly, the plane-strain ratio D reaches the level $D = 1$, indicating plane strain conditions, in the stress change field, at the rupture tip. This region is more extended for the case of $h = 20$ mm, even considering non-dimensional values of the x_3/h (Figs. 14d and 15d). Behind the rupture tip, both quantities reach a maximum with a small and more extended plateau in the case of $h = 10$ and 20 mm, respectively (Figs. 14 and 15). In the case of larger specimen, besides the plateau there is also a small dip in both σ_{33} and D at the midplane. The out-of-plane stress reaches the highest values at this cross-section, while the stress ratio D is below one here, indicating a fully three-dimensional stress state behind the rupture tip.

4. Conclusions

The stress state in plates is often assumed to be plane stress, due to the out-of-plane stress components satisfying the free-surface boundary conditions, and to the small thickness compared to other plate dimensions. This simplifying assumption has practical experimental implications in obtaining the out-of-plane components using a 2D measurement approach, as out-of-plane displacements could be computed directly from the in-plane components under plane-stress conditions. The present three dimensional finite element simulations show that dynamic rupture propagation perturbs the pre-existing plane-stress state with the development of marked out-of-plane stresses in the interior of the plate, particularly in the near-rupture tip. The stress state in the interior affects the in-plane displacements and particle velocities on the outer surface. The practical consequence is that out-of-plane displacements cannot be simply obtained from the in-plane components but need integration of the three-dimensional stress state in the interior, or direct measurement through a 3D system. These simulations emphasize the effect of the out-of-plane stresses even for plates of such small thicknesses, where the presence of σ_{33} contributes to modify the in-plane displacements and particle velocities.

The out-of-plane stress field on the interface plane presents complex features, with sharp variations over the plane-stress and free-surface condition immediately behind the rupture tip. These initial variations are followed by a crisscrossing pattern intensifying as the rupture develops. The degree of plane strain defined over the stress changes $D = |\tilde{\sigma}_{33}/(\nu\,(\tilde{\sigma}_{11} + \tilde{\sigma}_{22}))|$ provides a measure of the stress three-dimensionality in the near-rupture tip. Mapping the ratio D over the interface plane reveals rapid deviations from plane-stress conditions at the rupture tip, with plane-strain-like conditions in the stress changes establishing at the rupture front, and then evolving into a fully three-dimensional stress state behind the rupture tip. Interestingly, while D has its maximum at the rupture tip, the out-of-plane stress reaches its maximum at some distance behind the rupture front. The stress conditions revert to plane stress after a distance behind the rupture front equal to several times the plate thickness, indicating a more pronounced effect of dynamic ruptures compared to previous studies of static cracks, where plane-stress conditions are recovered half a thickness away from the crack tip.

The particle velocity and shear stress pattern on the interface plane is complex and reveals marked features crisscrossing the interface. While the predominant motion is in the interface-parallel direction, the anti-symmetric out-of-plane velocity field produces an out-of-plane slip rate, which would not be predicted under pure plane-strain conditions, but would be expected under plane-stress condition, though with a different magnitude. Previous experimental measurements of dynamic ruptures in plates showed a characteristic double-peak profile in the slip rate, for ruptures propagating at supershear speeds. This feature was attributed to the formation of shear Mach fronts propagating through the thickness of the specimen and which would result in a second peak in slip rate. Particle velocity measurements performed on plates of various thickness were consistent with this interpretation. However, previous numerical simulations typically assumed 2D stress conditions and did not show the double-peak effect which is a result of the finite plate thickness. The present finite-element simulations verify this hypothesis, for plates of two different thicknesses, by showing the inner structure of the discontinuity features, not accessible to experimental measurements.

Declaration of competing interest

The authors declare that they have no known competing financial interests or personal relationships that could have appeared to influence the work reported in this paper.

Acknowledgments

V.R. and A.J.R. would like to acknowledge the support of NSF, USA (Grant EAR-2045285 and EAR-1651235), the US Geological Survey (USGS) (Grant G20AP00037), the Geomechanics and Mitigation of Geohazard (GMG) Center at Caltech, USA (Project 6.2), and the Southern California Earthquake Center (SCEC), USA. SCEC is funded by NSF, USA Cooperative Agreement EAR-1033462 and USGS, USA Cooperative Agreement G12AC20038. J.F.M and R.R. acknowledge support from EPFL, Switzerland via internal funds.

References

Andrews, D.J., 1976. Rupture velocity of plane strain shear cracks. J. Geophys. Res. 81 (32), 5679–5687.

Barras, F, Aldam, M, Roch, T, Brener, EA, Bouchbinder, E, Molinari, J-F, 2019. Emergence of cracklike behavior of frictional rupture: the origin of stress drops. Phys. Rev. X 9 (4), 041043.

Barras, F, Aldam, M, Roch, T, Brener, EA, Bouchbinder, E, Molinari, J-F, 2020. The emergence of crack-like behavior of frictional rupture: Edge singularity and energy balance. Earth Planet. Sci. Lett. 531, 115978.

Bayart, E., Svetlizky, I., Fineberg, J., 2016. Fracture mechanics determine the lengths of interface ruptures that mediate frictional motion. Nat. Phys. 12 (2), 166–170.

Ben-David, O., Cohen, G., Fineberg, J., 2010. The dynamics of the onset of frictional slip. Science 330 (6001), 211–214.

Bouchon, M, Bouin, M-P, Karabulut, H, Toksoz, MN, Dietrich, M, Rosakis, AJ, 2001. How fast is rupture during an earthquake? New insights from the 1999 Turkey earthquakes. Geophys. Res. Lett. 28 (14), 2723–2726.

Brown, K.M., Fialko, Y., 2012. 'Melt welt'mechanism of extreme weakening of gabbro at seismic slip rates. Nature 488 (7413), 638–641.

Brun, M., Rezakhani, R., Molinari, J.-F., 2020. Explicit dynamic approach for unbounded domains in frictional contact with rate and state laws. Finite Elem. Anal. Des. 174, 103402.

Burridge, R., 1973. Admissible speeds for plane-strain self-similar shear cracks with friction but lacking cohesion. Geophys. J. Int. 35 (4), 439–455.

Coker, D., Lykotrafitis, G., Needleman, A., Rosakis, A.J., 2005. Frictional sliding modes along an interface between identical elastic plates subject to shear impact loading. J. Mech. Phys. Solids 53 (4), 884–922.

Dedontney, N, Templeton, E, Bhat, H, Dmowska, R, Rice, JR, 2008. Criteria for seismic splay fault activation during subduction earthquakes. In: AGU Fall Meeting Abstracts, Vol. 2008, T11D–02.

Di Toro, G, Han, R, Hirose, T, De Paola, N, Nielsen, S, Mizoguchi, K, Ferri, F, Cocco, M, Shimamoto, T, 2011. Fault lubrication during earthquakes. Nature 471 (7339), 494–498.

Dieterich, J.H., 2007. Treatise on Geophysics, second ed. Elsevier, Oxford, pp. 93–110.

Ellsworth, WL, Celebi, M, Evans, JR, Jensen, EG, Kayen, R, Metz, MC, Nyman, DJ, Roddick, JW, Spudich, P, Stephens, CD, 2004. Near-field ground motion of the 2002 Denali fault, Alaska, earthquake recorded at pump station 10. Earthq. Spectra 20 (3), 597–615.

Fekak, F, Barras, F, Dubois, A, Spielmann, D, Bonamy, D, Geubelle, PH, Molinari, JF, 2020. Crack front waves: A 3d dynamic response to a local perturbation of tensile and shear cracks. J. Mech. Phys. Solids 135, 103806.

Fineberg, J., Bouchbinder, E., 2015. Recent developments in dynamic fracture: some perspectives. Int. J. Fract. 196 (1–2), 33–57.

Freund, L.B., 1998. Dynamic Fracture Mechanics. Cambridge University Press.

Gabuchian, V, Rosakis, AJ, Bhat, HS, Madariaga, R, Kanamori, H, 2017. Experimental evidence that thrust earthquake ruptures might open faults. Nature 545 (7654), 336–339.

Goldsby, D.L., Tullis, T.E., 2011. Flash heating leads to low frictional strength of crustal rocks at earthquake slip rates. Science 334 (6053), 216–218.

Gori, M., Rubino, V., Rosakis, A.J., Lapusta, N., 2018. Pressure shock fronts formed by ultra-fast shear cracks in viscoelastic materials. Nature Commun. 9 (1), 1–7.

Ikari, M.J., Marone, C., Saffer, D.M., 2011. On the relation between fault strength and frictional stability. Geology 39 (1), 83–86.

Kammer, D.S., Radiguet, M., Ampuero, J.-P., Molinari, J.-F., 2015. Linear elastic fracture mechanics predicts the propagation distance of frictional slip. Tribol. Lett. 57 (3), 1–10.

Kanamori, H., Brodsky, E.E., 2004. The physics of earthquakes. Rep. Progr. Phys. 67 (8), 1429.

Kanamori, H., Rivera, L., 2006. Energy partitioning during an earthquake.

Lee, Y.J., Rosakis, A.J., 1993. Interfacial cracks in plates: a three-dimensional numerical investigation. Int. J. Solids Struct. 30 (22), 3139–3158.

Liu, X., Chen, G.S., 2016. Friction Dynamics: Principles and Applications. Woodhead Publishing.

Liu, Y., Lapusta, N., 2008. Transition of mode II cracks from sub-Rayleigh to intersonic speeds in the presence of favorable heterogeneity. J. Mech. Phys. Solids 56 (1), 25–50.

Lu, X., Lapusta, N., Rosakis, A.J., 2009. Analysis of supershear transition regimes in rupture experiments: the effect of nucleation conditions and friction parameters. Geophys. J. Int. 177 (2), 717–732.

Lu, X., Rosakis, A.J., Lapusta, N., 2010. Rupture modes in laboratory earthquakes: Effect of fault prestress and nucleation conditions. J. Geophys. Res.: Solid Earth 115 (B12).

Mello, M., Bhat, H.S., Rosakis, A.J., 2016. Spatiotemporal properties of sub-Rayleigh and supershear rupture velocity fields: Theory and experiments. J. Mech. Phys. Solids 93, 153–181.

Mello, M., Bhat, H.S., Rosakis, A.J., Kanamori, H., 2010. Identifying the unique ground motion signatures of supershear earthquakes: Theory and experiments. Tectonophysics 493 (3–4), 297–326.

Needleman, A., 1999. An analysis of intersonic crack growth under shear loading.

Passelegue, FX, Schubnel, A, Nielsen, S, Bhat, HS, Madariaga, R, 2013. From sub-Rayleigh to supershear ruptures during stick-slip experiments on crustal rocks. Science 340 (6137), 1208–1211.

Rezakhani, R., Barras, F., Brun, M., Molinari, J.-F., 2020. Finite element modeling of dynamic frictional rupture with rate and state friction. J. Mech. Phys. Solids 103967.

Rice, J.R., 1983. Constitutive relations for fault slip and earthquake instabilities. In: Instabilities in Continuous Media. Springer, pp. 443–475.

Rosakis, A.J., Krishnaswamy, S., Tippur, H.V., 1990. On the application of the optical method of caustics to the investigation of transient elastodynamic crack problems: limitations of the classical interpretation. Opt. Lasers Eng. 13 (3–4), 183–210.

Rosakis, A.J., Ravi-Chandar, K., 1986. On crack-tip stress state: an experimental evaluation of three-dimensional effects. Int. J. Solids Struct. 22 (2), 121–134.

Rosakis, A.J., Rubino, V., Lapusta, N., 2020. Recent milestones in unraveling the full-field structure of dynamic shear cracks and fault ruptures in real-time: From photoelasticity to ultrahigh-speed digital image correlation. J. Appl. Mech. 87 (3).
Rosakis, A.J., Samudrala, O., Coker, D., 1999. Cracks faster than the shear wave speed. Science 284 (5418), 1337–1340.
Rosakis, A.J., Samudrala, O., Singh, R.P., Shukla, A., 1998. Intersonic crack propagation in bimaterial systems. J. Mech. Phys. Solids 46 (10), 1789–1814.
Rosakis, A.J., Xia, K., Lykotrafitis, G., Kanamori, H., 2007. Dynamic shear rupture in frictional interfaces: Speeds, directionality, and modes.
Rubino, V, Lapusta, N, Rosakis, AJ, Leprince, S, Avouac, JP, 2015. Static laboratory earthquake measurements with the digital image correlation method. Exp. Mech. 55 (1), 77–94.
Rubino, V., Rosakis, A.J., Lapusta, N., 2017. Understanding dynamic friction through spontaneously evolving laboratory earthquakes. Nature Commun. 8, 15991.
Rubino, V., Rosakis, A.J., Lapusta, N., 2019. Full-field ultrahigh-speed quantification of dynamic shear ruptures using digital image correlation. Exp. Mech. 59 (5), 551–582.
Rubino, V., Rosakis, A.J., Lapusta, N., 2020. Spatiotemporal properties of sub-Rayleigh and supershear ruptures inferred from full-field dynamic imaging of laboratory experiments. J. Geophys. Res.: Solid Earth 125 (2), e2019JB018922.
Rubinstein, S.M., Cohen, G., Fineberg, J., 2004. Detachment fronts and the onset of dynamic friction. Nature 430 (7003), 1005–1009.
Scholz, C.H., 2019. The Mechanics of Earthquakes and Faulting. Cambridge University Press.
Shi, Zheqiang, Ben-Zion, Yehuda, Needleman, Alan, 2008. Properties of dynamic rupture and energy partition in a solid with a frictional interface. J. Mech. Phys. Solids 56 (1), 5–24.
Svetlizky, Ilya, Albertini, Gabriele, Cohen, Gil, Kammer, David S, Fineberg, Jay, 2020. Dynamic fields at the tip of sub-Rayleigh and supershear frictional rupture fronts. J. Mech. Phys. Solids 137, 103826.
Tal, Y., Rubino, V., Rosakis, A.J., Lapusta, N., 2019. Enhanced digital image correlation analysis of ruptures with enforced traction continuity conditions across interfaces. Appl. Sci. 9 (8), 1625.
Tal, Y., Rubino, V., Rosakis, A.J., Lapusta, N., 2020. Illuminating the physics of dynamic friction through laboratory earthquakes on thrust faults. Proc. Natl. Acad. Sci. 117 (35), 21095–21100.
Templeton, E, Baudet, A, Bhat, H, Dmowska, R, Rice, JR, Rosakis, AJ, Rousseau, CE, 2009. Finite element simulations of dynamic shear rupture experiments and dynamic path selection along kinked and branched faults.
Tippur, H.V., 1990. Mapping elasto-plastic deformations using optical and finite element methods.
Tsai, J.H., Patra, A., Wetherhold, R., 2005. Finite element simulation of shaped ductile fiber pullout using a mixed cohesive zone/friction interface model. Composites A 36 (6), 827–838.
Xia, K., Rosakis, A.J., Kanamori, H., 2004. Laboratory earthquakes: The sub-Rayleigh-to-supershear rupture transition. Science 303 (5665), 1859–1861.
Zehnder, A.T., Rosakis, A.J., 1990. Dynamic fracture initiation and propagation in 4340 steel under impact loading. Int. J. Fract. 43 (4), 271–285.